Advances in Physics: X

ISSN: 2374-6149 (Online) Journal homepage: www.tandfonline.com/journals/tapx20

Ultrashort field emission in metallic nanostructures and low-dimensional carbon materials

D. J. Park & Y. H. Ahn

To cite this article: D. J. Park & Y. H. Ahn (2020) Ultrashort field emission in metallic nanostructures and low-dimensional carbon materials, Advances in Physics: X, 5:1, 1726207, DOI: 10.1080/23746149.2020.1726207

To link to this article: https://doi.org/10.1080/23746149.2020.1726207

© 2020 The Author(s). Published by Informa UK Limited, trading as Taylor & Francis Group.

Published online: 16 Feb 2020.

Submit your article to this journal

Article views: 2617

View related articles

View Crossmark data

Citing articles: 4 View citing articles

Full Terms & Conditions of access and use can be found at
https://www.tandfonline.com/action/journalInformation?journalCode=tapx20

ADVANCES IN PHYSICS: X
2020, VOL. 5, NO. 1, 1726207
https://doi.org/10.1080/23746149.2020.1726207

Taylor & Francis
Taylor & Francis Group

OPEN ACCESS Check for updates

Ultrashort field emission in metallic nanostructures and low-dimensional carbon materials

D. J. Park[a,b*] and Y. H. Ahn[c*]

[a]School of Nano Convergence Technology, Hallym University, Chuncheon, Republic of Korea; [b]Hallym University, Laboratory of Nano Convergence Technology, Chuncheon, Korea; [c]Department of Physics and Department of Energy System Research, Ajou University, Suwon, Korea

ABSTRACT

This study investigates recent advances in photoelectron emission generated by irradiating ultrashort lasers on metallic nanostructures and low-dimensional carbon materials. Recently, primary focus has been on improving the efficiency of emitters, i.e. increasing the number of field-emitted electrons and their respective kinetic energies. An example of this is the modification of the conventional metal nanotip through adiabatic nanofocusing and various plasmonic metal structures, such as nanorods and bowtie antenna. The coherent emission control with two color irradiation enabled modulation in the emission yield. In addition, THz waves near the metallic nanostructure induced a highly accelerated, monochromatic energy. Alternative to metallic nanotips, carbon nanotubes are emerging as efficient photoelectron emitters, due to the large enhancement factor associated with their high aspect ratio and damage threshold. They particularly allowed the use of femtosecond light sources with a relatively short wavelength, resulting in the generation of photoelectrons with a narrow bandwidth. Additionally, electronic control over the single-walled nanotubes band structure added a degree of freedom for controlling the electron emission yield. Finally, we review the strong-field tunneling emission in graphene edge, with the emission yield showing an anomalous increase of nonlinear order, corresponding to the deep strong tunneling regime.

ARTICLE HISTORY
Received 15 November 2019
Accepted 28 January 2020

KEYWORDS
Photoionization; ultrafast processes; carbon nanostructures

CONTACT D. J. Park doojaepark@hallym.ac.kr School of Nano Convergence Technology, Hallym University, Hallymdaehaggil 1, Chuncheon 24252, Korea; Y. H. Ahn ahny@ajou.ac.kr Department of Physics and Department of Energy System Research, Ajou University, Suwon, Korea

*These authors contributed equally to this work.

This article has been republished with minor changes. These changes do not impact the academic content of the article.

© 2020 The Author(s). Published by Informa UK Limited, trading as Taylor & Francis Group.
This is an Open Access article distributed under the terms of the Creative Commons Attribution License (http://creativecommons.org/licenses/by/4.0/), which permits unrestricted use, distribution, and reproduction in any medium, provided the original work is properly cited.

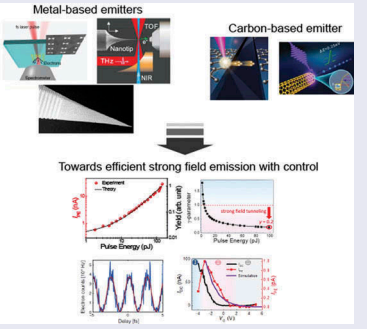

I. Introduction

High-energy electron generation with sub-picosecond pulse duration, using ultrafast lasers in the extra high-intensity regime, has been an active field of research, due to its potential application in high harmonic generation (HHG) [1–3], extreme-ultraviolet (EUV) generation [4–7], time-resolved electron microscope [8, 9], and attosecond electron pulse generation [10–15]. Coherent soft-X-rays of an extremely short pulse duration have been produced using a high-powered femtosecond laser in gas, cluster, and solid systems [16]. In addition, attosecond pulse generation and its streaking have been extensively investigated to achieve the temporal resolution of ~50 attoseconds [17–22]. This enables us to observe electron dynamics in atomic or subatomic systems, revealing atomic electron dynamics, nanoplasmonic field evolution, and attosecond scale tunneling delay [19,22–24]. Recently, the invention of ultrafast electron microscope and ultrafast low-energy electron diffraction microscopy made it possible to address real-time carrier motion and ultrafast structural dynamics [8, 9, 25].

The electron photoemission in various atomic and solid-state systems, induced by high-intensity laser irradiation, has conventionally been classified into two regimes: multiphoton ionization (MPI) (including the above-threshold ionization) [26–28] and strong-field tunneling [29, 30]. The Keldysh parameter, $\gamma = \omega\sqrt{2m_e I_p}/eE$ is widely accepted as an important criterion [31], where I_p is the ionization potential, m_e is the electron rest mass, e is the elementary charge, E is the peak electric field strength, and ω the angular frequency. Thus, $\gamma \approx 1$ is regarded as a critical value dividing the multiphoton ionization regime ($\gamma \gg 1$) and strong-field tunneling (i.e. optical field emission) regime ($\gamma \ll 1$) [32]. The electron–photon interaction in these two regimes is qualitatively different. In the MPI regime, the electron yield follows the N-th power of the laser intensity, where N is the nonlinear order in the absorption processes (see Figure 1(a)). However, in the strong-field tunneling regime, efficient electron barrier penetration is

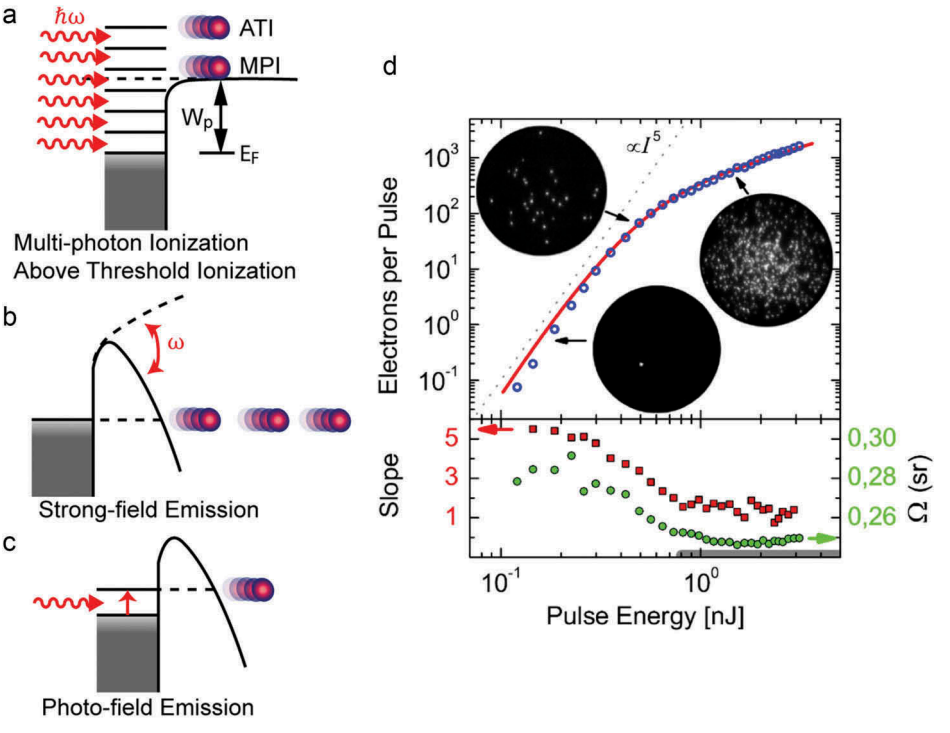

Figure 1. Schematic diagram of various electron emission mechanism of (a) multi-photon and above-threshold ionization (b) optical field emission (c) photo-field emission (d) Photoelectron emission from a sharp metal tip as a function of pulse energy. Copyright Physical Review Letters, American Physical Society [58].

predominantly caused by a narrowing of the vacuum barrier due to the oscillating electric field of the irradiating laser as shown in Figure 1(b). Under the influence of a strong laser field, the vacuum barrier allows penetration only in a short period of time for each cycle of the laser oscillation; hence, the time duration of generated electron wavepackets is within the half cycle of the incident laser field. In particular, the use of an ultrafast few-cycled laser generated a single bunch of electron wavepackets with a sub-femtosecond time duration. This is essential for the attosecond streaking system required for investigating atomic scale time dynamics [33]. Conversely, in a photo-field emission process, the amount of tunneling electron is mediated by the photo-induced excitation of Fermi electrons as shown in Figure 1(c). In the presence of a static electric field, the photo-excited electrons face a much narrower tunnelling barrier, resulting in a highly enhanced emission current, in which the subcycle emission (as found in the optical field emission) is hardly expected.

The degree of motion is characterized by the ponderomotive potential $U_p = e^2E^2/4m_e\omega^2$, which is the average energy gained by the electron from the laser field, during one field oscillation cycle [34–36]. Higher

ponderomotive potential is preferred for efficient HHG and attosecond streaking, which can be obtained using light sources of lower frequency and higher peak electric field amplitude. For example, considering that the cutoff energy of HHG is 3.17 U_p [26], conventional EUV generation of wavelength ~13 nm requires the peak electric field of the pulsed laser to be ~60 GV·m^{-1} (corresponding to the peak intensity of ~3 ×10^{14} W·cm^{-2}) at a wavelength of 800 nm. Achieving the large ponderomotive potential is also important in time-resolved studies in atomic scale using attosecond streaking [37, 38]. This regime has conventionally been achieved by irradiating the ultra-high intensity laser on an atomic jet or metal vapor, requiring a multi-stage amplifier.

Novel phenomena of electromagnetic field enhancement in the near-field region can inspire many interesting research areas, such as plasmonics [39–44], surface-enhanced Raman scattering [45–47], single molecule detection [48, 49], and metamaterials [50–54]. In those research topics, field enhancement and associated field confinement are considered essential to achieve high sensitivity detection within the subwavelength spatial resolution. Huge field enhancement near metallic nanostructures has enabled electron ionization using light sources of relatively low intensity. Both multiphoton ionization [55–57] and strong-field photoemission [58] have been manifested using laser field irradiation with intensity <1 GW·cm^{-2}. The transition from MPI to strong-field tunneling at $\gamma \approx 2$ was confirmed by the distinct decrease of nonlinear order in the electron generation yield, as a function of the incident laser pulse energy (see Figure 1(d)). These results suggest that strong-field physics can be achieved with low-intensity light due to near-field enhancement in nanostructures. Another distinguishing feature for the strong-field tunneling in nanostructures is symmetry breaking, which is beneficial to ultrashort pulse generation. For example, in a metallic nanotip, the electric force exerted on the tip apex, $\vec{F} = -e\vec{E}$, contributes to electron tunneling only when it is directed towards the vacuum, due to the incident laser field oscillation [59]. This implies that the electron wavepacket generated by strong-field tunneling has a temporal width corresponding to the half cycle of the incident laser field, e.g. a pulsewidth of the order of hundreds of attoseconds can be achieved when a near-infrared light source is used [60–62].

Even though strong-field tunneling emissions have been successfully explored using metal nanoprobes or metal nanostructures [55, 57, 58, 60, 63–70], they have been limited in terms of achieving a large ponderomotive potential, due to the thermal damage that frequently leads to the meltdown of nanostructures [67]. This will also restrict the possible quantity of ultrashort electron emissions from the metal nanotip [69, 71]. Their functionality is minimally variable, and therefore, the control of electron motion has been primarily manifested by varying the

geometry of the metal structure (such as the tip apex and conical angles) and the physical properties of the laser [60–62, 72, 73]. The development of novel, functional devices are required to achieve the unprecedented control for the subcycle electron yield, the maximum kinetic energy of electrons, and an efficient emission direction. Low-dimensional carbon materials, such as graphene and carbon nanotubes (CNTs), have nanoscale morphology capable of producing high emission current density due to their high damage threshold [74–77]. Therefore, they potentially serve as an ideal platform for ultrafast field emission devices in the strong tunneling regime due to their high aspect ratio, high carrier density, larger carrier mobility, and mechanical stability.

In this article, we present an overview on contemporary advancement in ultrashort laser-induced tunneling in various nanostructures including low-dimensional carbon materials. In section II, we introduce recent developments in strong-field photoemission using advanced metallic nanostructures for the improved emission rate. This will include grating-coupled tips, nanorods, and bow-tie antenna. We also discuss theoretical approaches, such as the role of near-field distribution around the metal tip and the novel dynamic aspects of photoemission in the presence of a strong DC field. A brief introduction to DC field emission in various CNT systems will be presented in Section III, followed by a discussion on strong-field tunneling emission in CNTs. This includes strong-field tunneling emission with a narrow spectral energy and short wavelength excitation, the observation of extreme nonlinearity, and the electronic switching of the photoemission. Finally, in Section IV, we review the photoemission occurring in graphene edges, specifically in graphene nanogap devices, in which the unprecedented Keldysh parameter has been obtained in the near-infrared range.

II. Photoemission in metallic nanostructures

A. Dynamic motion of electrons near metallic nanostructures

The interesting dynamic motion of the photo-induced electrons has been revealed by introducing metallic nanostructures [61]. The electrons generated by the strong-field tunneling process exhibit a unique motion under a strong, oscillating laser field, referred to as a quiver motion. This is the back-and-forth movement of the photoemitted electrons in the nanometer-scale. The quiver amplitude, which is the characteristic length of the electron quiver oscillation, is directly related to the ponderomotive potential as $l_q = eE/m_e\omega^2 = 2\sqrt{m_e}U_p$. Enhancement of the electric field near the nanostructure is strongly localized, the length scale of which is directly correlated with the dimension of the nanostructures [78, 79]. Here, the degree of field localization is characterized by a field decay length l_F [61]. As the

nanostructures scale down, l_F significantly decreases, whereas the quiver amplitude l_q further increases. In this case, it is easy to reach the regime of $l_F < l_q$. Because the electrons escape the field enhancement region within a half cycle of its oscillation period for $l_F < l_q$, they no longer follow the quiver motion and exhibit a more straightforward movement. Such specific motion was possible by introducing the nanostructures and has been referred to as *sub-cycle motion* (see Figure 2(a)) [61]. When the electron is in the sub-cycle regime, it is suggested that the terminal kinetic energy exceeds the ponderomotive potential because they do not experience the deceleration occurring in the opposite half-cycle [61, 62].

An additional advantage of the strong-field emission from nanostructures is the steering of electron motion [62]. The electric field curvature associated with the nanostructure morphology enables the tailoring of electrons. There have been exceptional efforts made to unravel the electron dynamics in the vicinity of the highly confined, enhanced electric field, influenced by control parameters such as wavelength [61], field strength [58, 61, 62], and the carrier-envelop-phase difference [60, 63]. The change of the electron dynamics with carrier-envelop-phase (CEP) variation has been of particular interests (see Figure 2(b)). The net acceleration of the electrons emitted within the half-

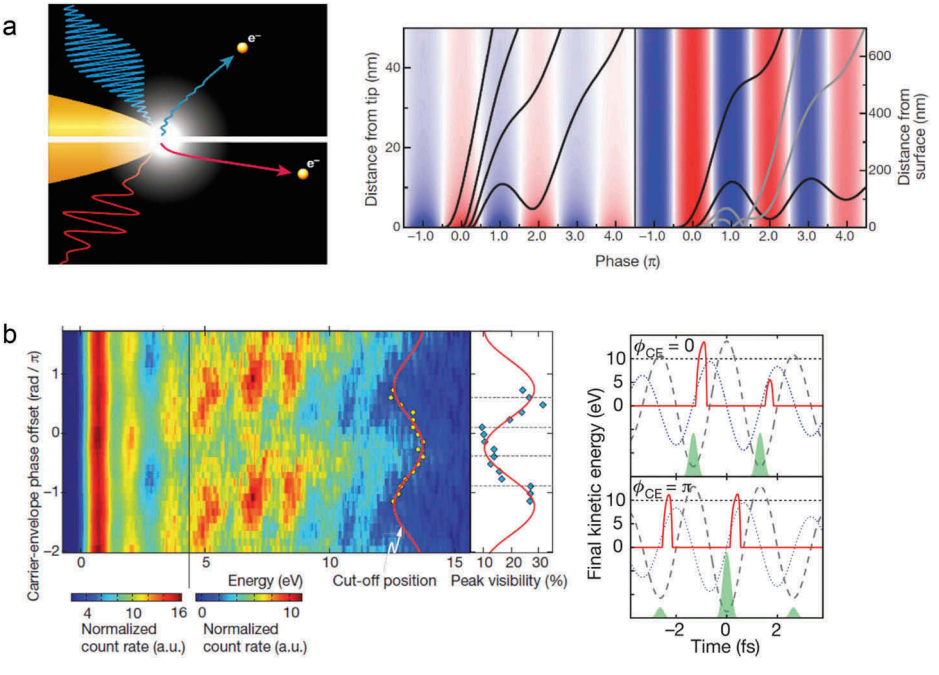

Figure 2. (a) Simulated photoelectron trajectories generated by intense light fields for four emission phases in localized (bottom left) and homogeneous (bottom right) pulsed fields. Copyright Nature, Nature Publishing Group [61] (b) Carrier-envelope phase modulation in photoelectron spectra and emission probability as a function of emission time. Copyright Nature, Nature Publishing Group [60].

cycle of the laser field differs when the few cycle pulses having different CEP are irradiated. Hence, variation of the maximum kinetic energy of the photoemitted electron is a strong evidence of the ultrashort, sub-cycle electron generation via strong field tunneling processes [60].

The sub-cycle emission and its motion near the metal nanostructures have been successfully analyzed using standard approaches such as the semi-classical calculation, the quantum mechanical calculation of electron wavepacket, and the first-principle calculation. In strong-field regime, the semi-classical approach (referred to as Simpleman model) has been widely adopted; the emission yield and its dynamics are calculated separately [56, 60, 80]. To calculate the emission yield, Fowler-Nordheim formalism is applied with respect to the time-varying laser field. Conversely, the electron dynamics is simulated using the Newton's equation of motion because the electron wavepacket can be regarded as a classical particle in sufficiently high ponderomotive potential. To simulate the dynamic motion more precisely, a time-dependent three dimensional Schrödinger equation has been incorporated; the solution has been given by a perturbative approach or by using numerical methods [81–83]. Importantly, this method can be applied both in the multiphoton regime and the strong field regime. Besides, a time-dependent density functional theory was applied to include the Coulomb interaction between the emitted electrons [84]. In many instances, the semi-classical Simpleman model has proven to be a very efficient tool for addressing the dynamic motions in strong-field tunneling regime and their results converge with those of the quantum mechanical approaches [60].

B. Improved photoelectron emission in metallic nanoprobes

By incorporating metallic nanoprobes for ultrashort photoelectron emission, the use of low-intensity light sources became available for table-top experiments. Additionally, unique dynamic behavior near the metal nanotips has been observed, providing novel functionality and controllability. The recent progress in the modification of nanotip morphology has significantly improved photoemission, because efficient near-field accumulation is manifested by adiabatic nanofocusing [78, 79, 85–87]. By using a grating-coupling technique for adiabatic nanofocusing of the pulsed laser, centered at 1600 nm with a peak electric field of 0.5 $V{\cdot}nm^{-1}$, as shown in Figure 3(a), the electron emission increased up to 50 times compared to the conventional method that is based on the direct illumination on the tip apex [66]. The resultant electric field, due to nanofocusing at the apex, was estimated to be ~6 $V{\cdot}nm^{-1}$, an order of magnitude higher than the conventional case. Using this nanoprobe electron source, the real-time imaging of charge separation in a nanoantenna system has been successfully demonstrated with a time resolution of ~25 fs, resulting in a new application for ultrafast nanostructure microscopy [88]. In addition, a suppressor and

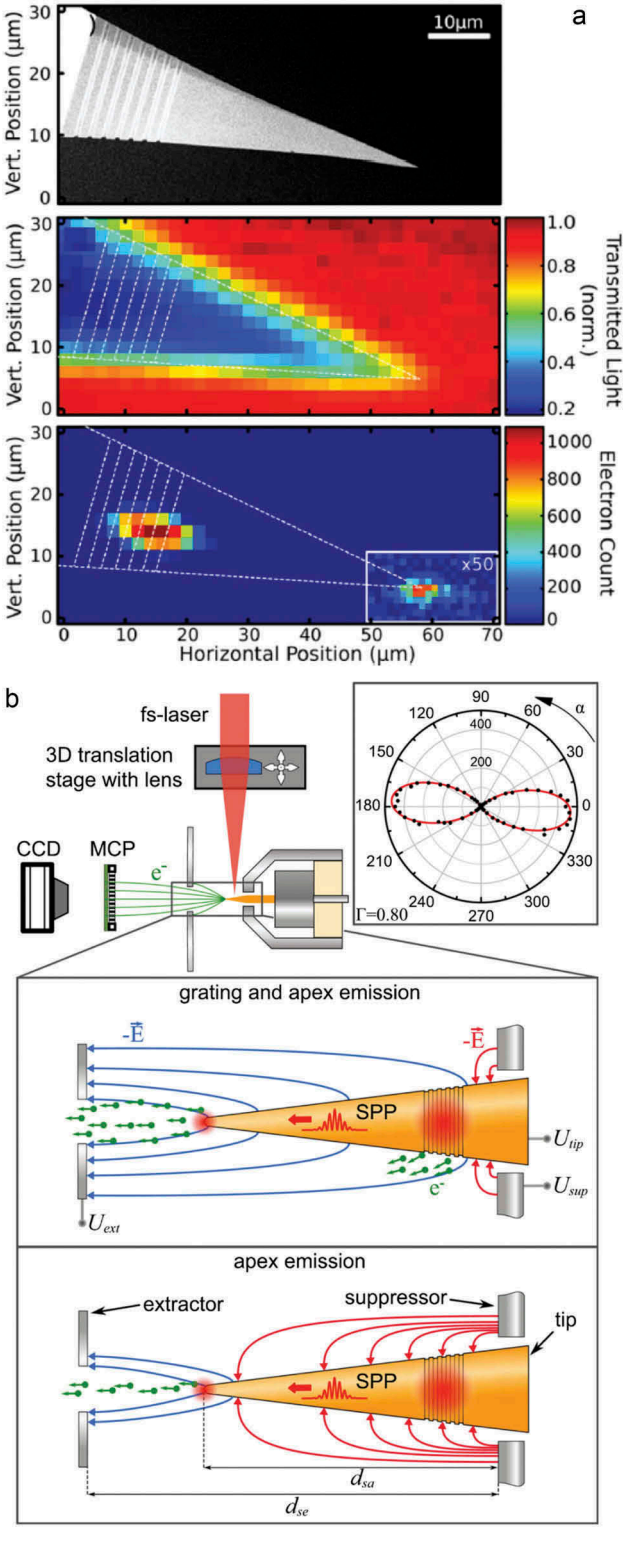

Figure 3. (a) Photoelectron emission from a gold nanotaper with a grating pattern when illuminated with a fs laser pulse centered at 1.6 μm. Copyright Nano Letters, American Chemical Society [66] (b) The gold tip in a suppressor-extractor-geometry allowing the efficient photoemission from the regions close to the apex. Copyright Applied Physics Letters, American Institute of Physics [89].

an extractor which surround the tips (with a grating) have been introduced to remove the unexpected photoelectrons emitted outside the tip apex area, as shown in Figure 3(b) [89]. This is useful in producing the pointwise, ultrashort electron sources for the development of next-generation ultrafast electron microscopes [38].

Detailed studies investigating the field distribution at the tip apex were carried out to achieve the optimal design for efficient photoelectron generation. Electron generation mechanism and its respective dynamic motion is significantly affected by the near-field distribution. It is well established that tip apex radius and opening angle is directly related to the field enhancement [72]. A recent theoretical study has thoroughly demonstrated these dependencies [90] by considering the complex dielectric function of gold, silver, aluminum, and tungsten. In this study, the tip radius was found to be a critical factor in the field enhancement. The field enhancement was studied as a function of the opening angle of the metal tip. The result showed that the enhancement effect is maximized at a certain optimal angle [90]. For example, at the radius of 5 nm, the field enhancement factor was measured to be ~12 for tungsten and ~35 for gold at the opening angle of ~40° and ~14°, respectively. Local surface plasmon excitation, the resonance of which depends on the geometry of the conical structure, has been attributed to the observed optimal field-enhancement conditions.

Alternative to the use of novel functionalized tips, the simultaneous irradiation of two color lasers has been proposed to achieve coherent emission control in individual nanotips, as shown in Figure 4(a) [91]. Here, the electron photoemission was modulated homogeneously over the entire emission channel with a 94% contrast, using strong femtosecond lasers with wavelengths centered at 1560 nm (ω) and 780 nm (2ω). The high contrast was attributed to the quantum-pathway interference between the 4-photon absorption and the 2-photon absorption accompanied by 1-photon absorption of 780 nm. Furthermore, two-color laser field irradiation was found to introduce a quenching of the electron backscattering and the variation of maximum kinetic energy, as shown in Figure 4(b) [92].

Considering the wavelength scaling law, THz waves were recently applied to achieve the lower Keldysh parameter and higher ponderomotive acceleration with a relatively low peak electric field. The strong-field electron emission was manifested in a sharply etched tungsten tip by high intensity THz field irradiation [93]. Here, high electron acceleration was achieved with terminal kinetic energy reaching ~120 eV at the relatively low THz field strength of 5.3 $V{\cdot}nm^{-1}$. This was obtained experimentally by applying the THz streaking method [94]. It is important to note that quasi-static acceleration of electrons was observed due to the slowly varying electric field of the THz wave; this is confirmed by the electron energy spectra with a sharp cutoff, as shown in Figure 4(c). The results suggest that the highly

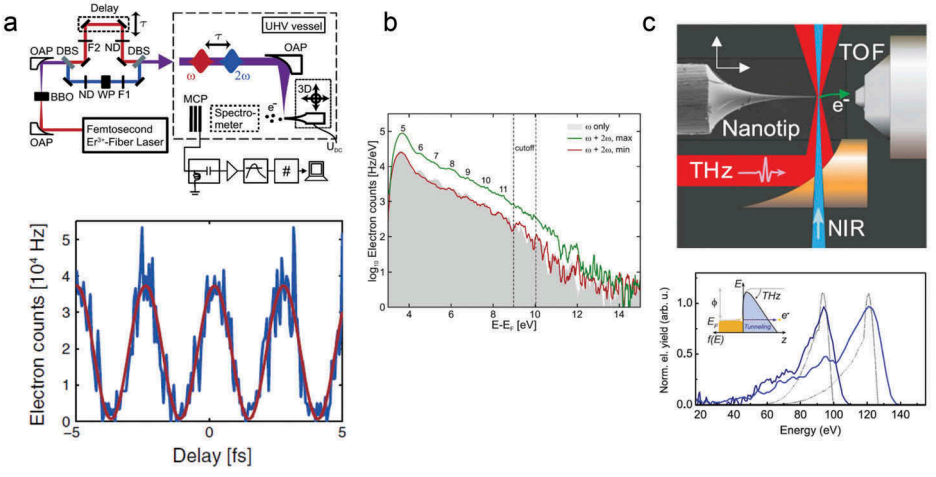

Figure 4. (a) Coherent control of strong-field tunneling emission by using two-color laser sources. Copyright Physical Review Letters, American Physical Society [91] (b) Measured electron energy spectra from a nanotip in a bichromatic laser field. Numbers indicate multi-photon orders of the fundamental. Copyright Journal of Physics B, IOP Publishing [92] (c) Subcycle electron emission using localized THz fields near the metal tips. Copyright New Journal of Physics, IOP Publishing [93].

accelerated, monochromatic electron emission is produced by using the THz waves, which will be beneficial for use in ultrafast electron microscopes [95, 96].

C. *Electron emission in various metallic structures*

Nanoplasmonic structures alternative to sharply etched metallic nanotips are also a promising candidate for strong-field photoemission. Multiphoton emission and strong-field photoemission were proven for a planar gold surface using mid-IR laser irradiation and a relatively low pulse intensity of less than 1 GW·cm^{-2}. This was confirmed by the abrupt decrease of the local slope in the power-dependent photocurrent measurement below the multiphoton order (see Figure 5(a)) [97]. Moreover, the maximum kinetic energy was measured as high as 47 eV at 3.5 GW·cm^{-2}, which scales well with the classical ponderomotive cutoff law (see Figure 5(b)). Conversely, probing the field enhancement due to the plasmon-plasmon coupling in a super-polished metal surface have shown the possibility for ultra-sensitive near-field probing and surface metrology [98]. Gold nanorods also served as strong-field electron emitters, when irradiated with mid-IR femtosecond pulses, having a pulse duration of 50 fs and a center wavelength varying from 3.5 μm to 8 μm [99]. Clear resonance behavior of the photoelectron yield confirms the field enhancement factor of 36 in resonant excitation conditions (see Figure 5(c)). Photoemission of electrons by MPI processes in

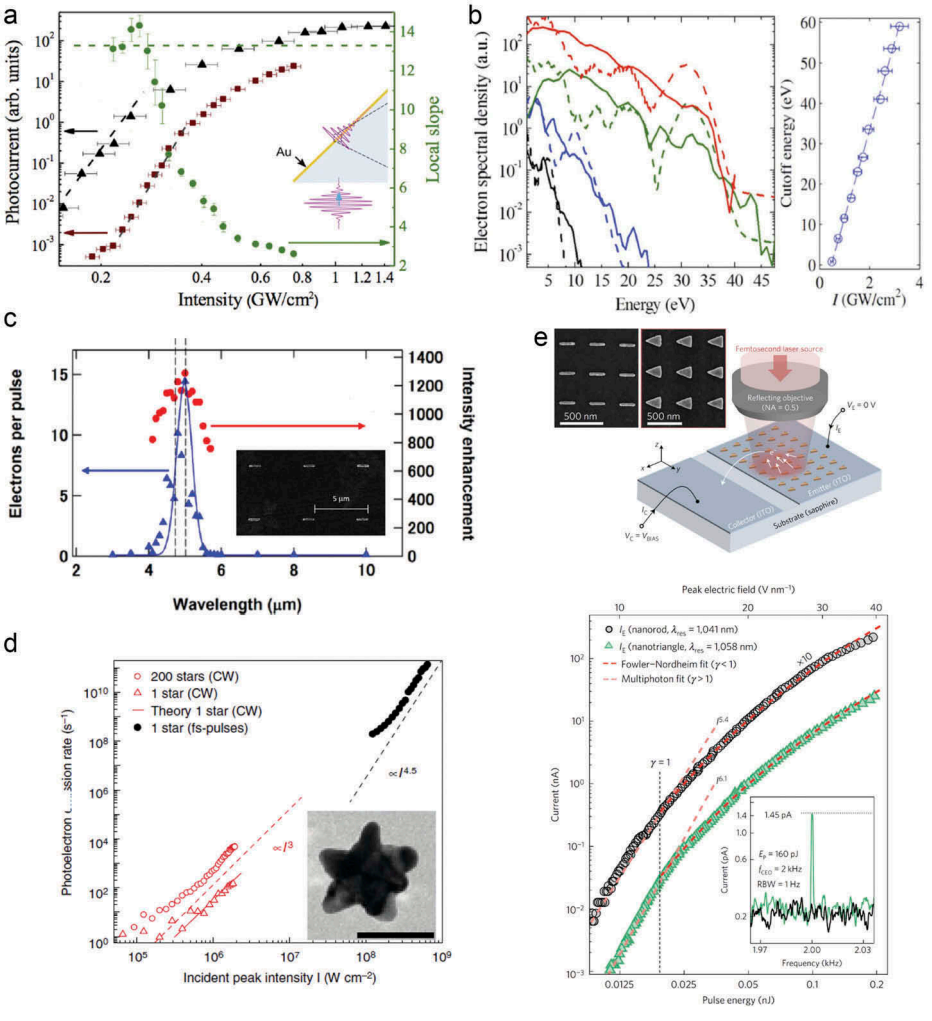

Figure 5. (a) Strong-field photoemission and electron acceleration in nanolocalized surface plasmon fields generated on thin gold films by focusing nine-cycle laser pulses in the Kretschmann-Raether coupling geometry. Copyright Scientific Reports, Nature Publishing Group [97] (b) Photoemission spectra (right) and maximum kinetic energy (left) of plasmonically accelerated photoelectrons for a planer gold structure. Copyright Scientific Reports, Nature Publishing Group [97] (c) Far-field extinction spectrum and intensity enhancement factors in an electron emission form a nanorod array (rod length of 1 μm). Copyright AIP Advances, American Institute of Physics [99] (d) An intensity dependence of the photoelectron emission rate for single and multiple nanostars. Copyright Communication Physics, Nature Publishing Group [100] (e) Transition of photoemission from multiphoton regime to strong field regime in individual nanoantennas with near-IR pulse irradiation. Copyright Nature Physics, Nature Publishing Group [101].

the plasmonic nanostar was also reported recently (see Figure 5(d)) [100]. Due to a high field enhancement factor up to 32, at the sharp edge of the nanostar, photoelectron generation was achieved using a continuous-wave source with an intensity of sub MW·cm^{-2}. In the near-IR range, strong-field

emission is also reported using localized plasmon resonant enhancement in nanoantennas as shown in Figure 5(e) [101]. Nanorod and nanotriangle arrays were exposed to the tightly focused femtosecond laser having a 10-fs time duration and a center wavelength of ~1 μm inside the vacuum. The emitter current as a function of the incident pulse implies the transition from the multiphoton regime ($\gamma > 1$) to the strong field regime ($\gamma < 1$), as depicted in the middle of Figure 5(e). Vanishing of the CEP sensitivity of the photoemission in the higher pulse energy condition has been observed (see right of Figure 5(e)), which has been attributed to the increasing contribution from the neighboring half cycle [102].

Among nanoplasmonic structures, bowtie structures were expected to provide a superior field enhancement factor, reaching ~50 [103]. Motivated by these advantages, EUV generation was demonstrated by exploiting the field enhancement effect present at the gap of the metallic bow-tie antenna [68]. Here, successful EUV generation with a wavelength as low as 47 nm was observed by injecting an Argon gas jet to the bow-tie metallic nanostructure with a ~20 nm gap. However, there is still a debate on whether the EUV generation is due to the high harmonic generation or the plasma radiation [67, 104, 105]. The results of the ultrafast field emission from a bow-tie antenna without the gas jet injection are shown in Figure 6(a) [106, 107]. The pronounced plateau in the photoelectron spectra confirms the existence of strong-field tunneling emission, which is a clear indication of sub-cycle acceleration of photoelectrons [61 62,]. Combining the maximum kinetic energy with the analysis on the electron dynamics, the field enhancement at the gap was measured up to 50. More recently, phase control of the electron tunneling in the bow-tie structure with an 8 nm gap has been reported using the CEP-stabilized short-pulse laser having a 6-fs pulsewidth (Figure 6(b)) [108]. In other words, the significant switching of photocurrent was observed with the variation of CEP difference, which confirms the individual electron transfer within a half-cycle period of ~2 fs. However, those metallic nanostructures suffer physical damage during high-intensity laser irradiation. For example, in bow-tie antenna, a meltdown was observed over the course of a few minutes of fs laser irradiation of 0.3 $TW \cdot cm^{-2}$ pulse intensity and a center wavelength of ~800 nm (see Figure 6(c))[67].

D. Electron emission in the presence of a strong DC field

Most of the previous experiments on ultrafast field emission have been performed in the absence of DC electric fields; the photoelectrons were measured by the anode electrode, which is located far from the cathode metal tip. In a number of recent studies, in which the photoemission occurred through a small gap [71, 109], a strong static field induced by

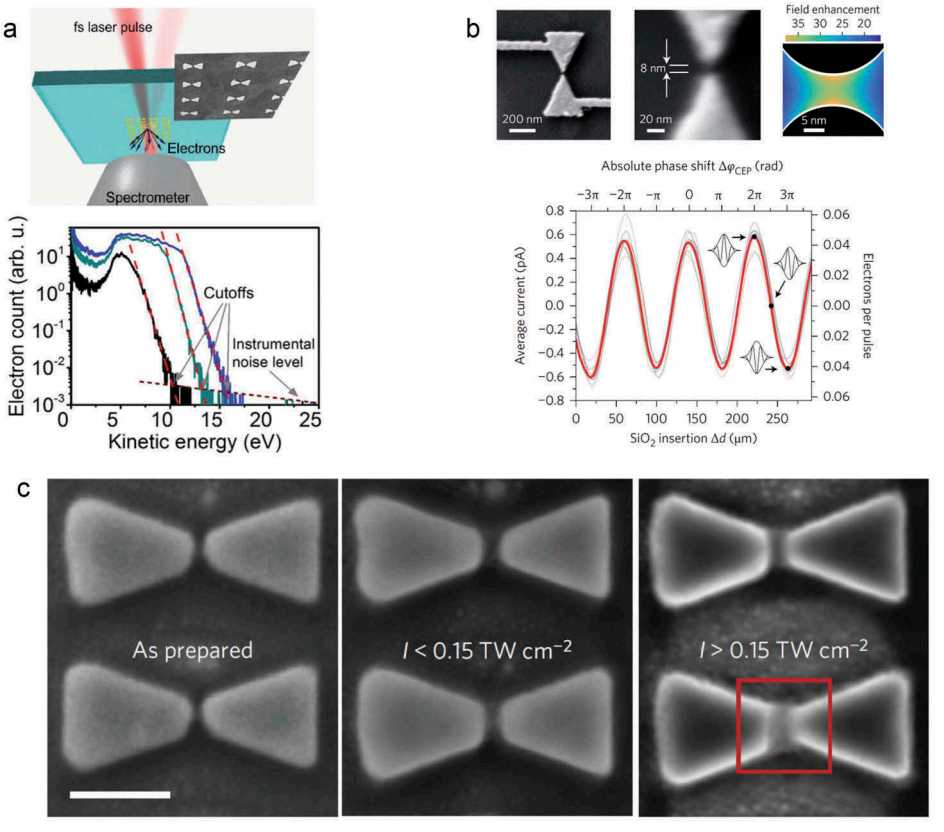

Figure 6. (a) Plasmonic photoelectron spectra emitted from bow-tie antenna structures. Copyright Nano Letters, American Chemical Society [107] (b) Carrier-envelope optical control of sub-cycle tunnelling in the nanoantenna. Copyright Nature Photonics, Nature Publishing Group [108] (c) A series of SEM images of bow-tie structure, after several hours of exposure to incident lights. Copyright Nature Physics, Nature Publishing Group [67].

a DC bias voltage across the gap significantly influences the emission efficiency and dynamic motion. In this case, while the DC field significantly narrows the vacuum level, the fs light triggers the photo-field emission by additional electronic bending or by thermal electron generation. Recently, an experimental study was done on the dynamics of the delayed electrons that are generated via re-scattering of quiver electrons in the presence of a large DC electric field [110]. By using a blunt tungsten tip, with a radius of ~100 nm and applying a high voltage of up to ~3300 V, they observed a combined contribution of the DC field and the strong laser field as depicted in Figure 7(a). Plateau broadening and peak shift in the energy spectra have been observed simultaneously as the incident laser field strength increases. This is consistent with the prediction based on channel broadening and the downshift of the multiphoton order.

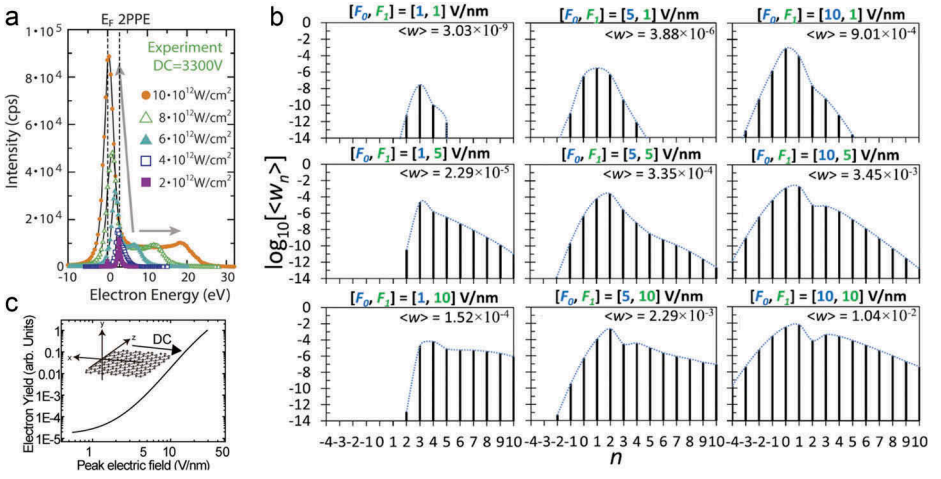

Figure 7. (a) Experimental energy spectra of field emission in the presence of large DC electric field. Scientific Reports, Nature Publishing Group [110] (b) Simulated, time-averaged normalized emission current density through the n-th channel, under various combination of DC electric field F_0 and laser field F_1. Copyright Scientific Reports, Nature Publishing Group [111] (c) Laser power dependence of the simulated electron emission yield in the presence of DC bias, based on a Simpleman model on two-dimensional metallic edge. Copyright Springer, Journal of the Korean Physical Society [113].

A theoretical investigation on the combined contribution of the DC electric field and the light field on the electron emission has been reported recently [111]. In this study, a time-dependent Schrödinger equation was solved to provide an exact solution for the laser field irradiating on a metal surface in the presence of a DC electric field. The solution was given as a superposition of electron plane waves with an energy of $\varepsilon + n\hbar\omega$, where ε is the fermi energy, $\hbar\omega$ is the incident photon energy, and n is the multi-photon order. The channel-resolved emission rate under various combinations of DC field and laser field were demonstrated (see Figure 7(b)). The photoemission through various multiphoton orders has been observed in the presence of a large DC field. It is important to note that this revealed a mechanism for photoexcited electron tunneling mediated by single- or multiphoton absorption, which is unique in the presence of the DC field [112].

A more simplified model of electron motion in a semi-classical limit has been developed recently, taking the DC field contribution into consideration [71]. Here, the photoelectron generation, and their subsequent motion, has been simulated with the assumption of two-dimensional metal edge structures, a theoretical counterpart for the graphene edge emitter, as will be discussed in Section IV. The total electron yield was calculated from the time-dependent Fowler–Nordheim equation, in the semiclassical limit, with the presence of a DC electric field. The recoil electrons were excluded when integrating the emission yields. It was found that the net photocurrent,

which is a summation of electrons that have successfully escaped from the near-field region, did not follow the traditional Fowler–Nordheim dependence as a function of the incident electric field's strength, as shown in Figure 7(c) [113]. Specifically, the nonlinear order increases as the electric field increases. This is because an increase in the electric field causes a decrease in the relative strength of the DC bias. Thus, the traditional Fowler–Nordheim dependence starts to dominate the photoemission. This is consistent with the experimental findings obtained in a graphene nanogap device, which will be discussed later.

III. Electron photoemission in carbon nanotubes

A. DC field emission in CNTs

Strong electric fields and the associated field gradients near sharp metallic nanostructures have enabled photoemission, based on strong-field tunneling with sufficiently low light intensity [56 65 114,,]. The control of electron motion by varying the intensity, wavelength, or carrier-envelop phase difference has been considered a key factor in ultrashort pulse generation and the maintenance of the respective pulse width during free space travel [60–63,73]. However, achieving a large ponderomotive potential requires a high-intensity laser field and a longer wavelength, reaching the mid-infrared range. Most previous studies on laser-induced electron emissions are based on metal nanoprobes [55–58, 60, 63, 64, 66], or similar metal nanostructures [67, 70], which suffer from thermal damages in the high-intensity regime. In addition, their functionality is mostly fixed; hence, electron motion has been primarily controlled by varying the physical properties of the laser and the geometry of the metal structure, such as the tip apex and conical angles.

Low-dimensional carbon materials, particularly CNTs, have been regarded as a potential candidate for DC electron field emitters due to their high electrical conductivity, large damage threshold, chemical stability, and high aspect ratio [115]. Detailed information on their synthesis, optoelectronic properties, and applications can be found in [116, 117]. Since the pioneering work by de Heer et al., their potential for field emission has increased for applications, such as displays, X-ray tubes, and microwave amplifiers [118]. This is because CNT field emission devices have the advantage of fast response, low energy consumption, and stable performance. Both single-walled nanotubes (SWNTs) and multi-walled nanotubes (MWNTs) have been demonstrated as field emission devices in the form of single-point emitters, vertically aligned bundles, and patterned films. Vertically aligned MWNTs synthesized by plasma-enhanced chemical vapor deposition (PECVD) are of particular importance for practical applications, as shown in Figure 8(a) [119]. A triode structure, with integrated gate electrode, was utilized to achieve the high switching rate and low-

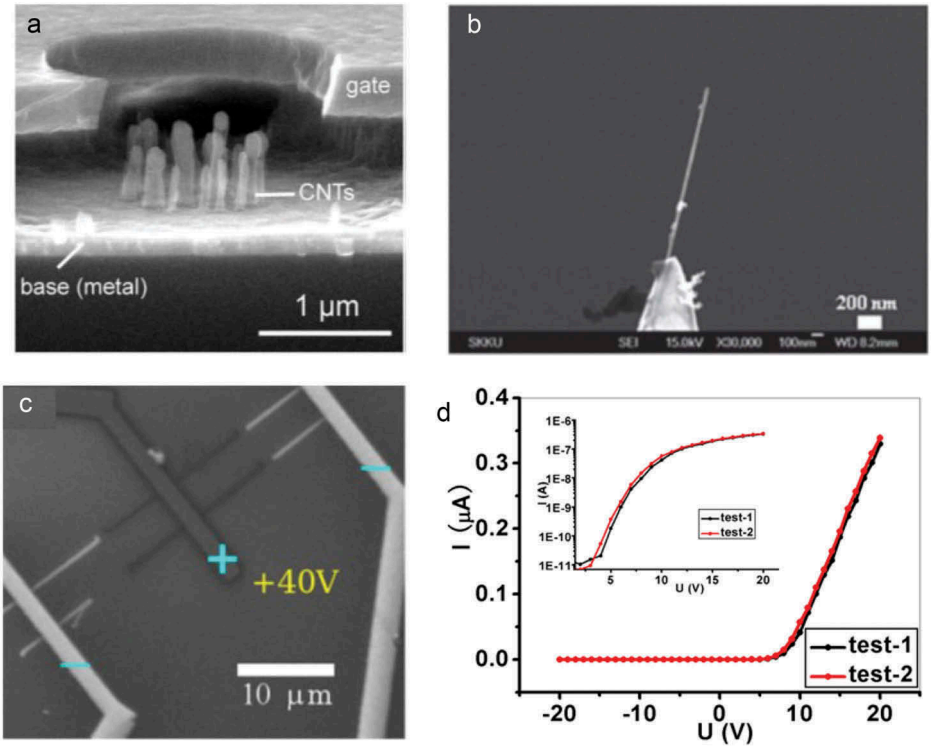

Figure 8. (a) Vertically aligned MWNT field emitter incorporated into a triode structure. Copyright Nanotechnology, IOP Publishing [119] (b) SEM image of an individual MWNT point emitter. Copyright Applied Physics Letters, American Institute of Physics; Diamond and Related Materials, Elsevier [120 121,] (c) and (d) A planar field emission device fabricated using as-grown individual CNT. Copyright Nanotechnology, IOP Publishing [122].

voltage field emission. There are several studies on the vertically aligned SWNTs and MWNTs arrays of different configurations. Most of these studies have reported emission currents ranging from 1 mA· cm^{-2} to 1 A· cm^{-2}. Conversely, single SWNT and MWNT emitters have been alternatively developed by attaching them on a metal tip using the electrophoresis method (see Figure 8(b)) [120, 121]. An emission current higher than 100 μA has been achieved from a single MWNT emitter, with a current density of ~ 10^7 A · cm^{-2}. In addition, a planar field emission device has been fabricated using as-grown individual CNTs on the surface of a Si substrate, as shown in Figure 8(c,d) [122]. The anode and cathode (with a CNT tip) lie on the same surface, which is beneficial for integration with planar technology, stable construction, and improved heat dissipation. In most applications, however, the single nanotube emitter is not only vulnerable but also incapable of providing a sufficiently high field emission current. Thus, it is applied less frequently than the planar CNT field emitters.

B. Ultrashort photoemission in SWNT with a narrow bandwidth

Generation of strong-field tunneling emission has been recently demonstrated in an SWNT system, which had an ultra-small tip radius of ~1 nm, using near-infrared (820 nm) and near UV (410 nm) fs lasers (Figure 9(a)) [123]. Although vertically aligned SWNT bundles were used, a few isolated, individual SWNTs protruded out of the as-grown cluster, which were believed to be the main photoemission sites with high field enhancement. The focused fs laser, with spot sizes of 1.25 μm and 2.50 μm (FWHM, 410 nm and 820 nm), illuminated the SWNT cathode, while the anode electrode (placed 400 μm above) collect the photoelectron emission in a high-vacuum chamber. Photoelectron emission was observed with a strong laser-polarization anisotropy. It is important to note that the transition from the multiphoton excitation regime to the field-driven regime has been observed in the plot of photoemission current as a function of laser power, as shown in Figure 9(b). An AC field-enhancement factor of 27 (for the excitation at 410 nm) has been estimated from the laser power dependence, as shown by the Fowler–

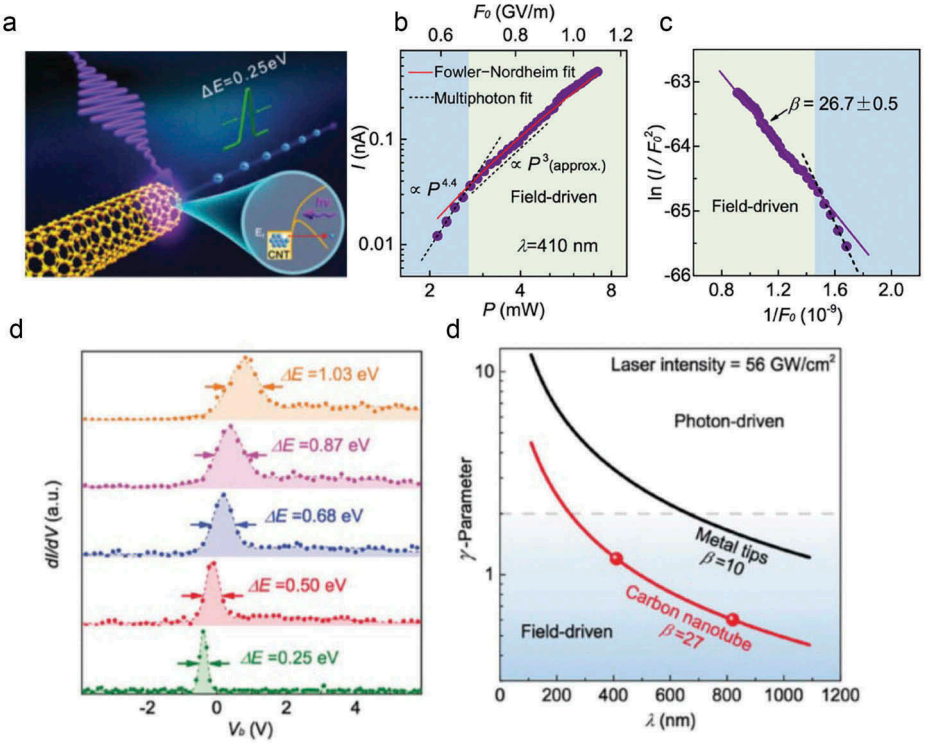

Figure 9. (a) Schematic of laser-induced field emission from an SWNT tip. (b) Photoemission as a function of laser power demonstrating a transition in nonlinear order. (c) Fowler-Nordheim plot of the laser field emission from the SWNT. (d) Kinetic energy spectra of photoelectron emission. (e) Keldysh parameter estimated from the enhancement factor. Copyright Advanced Materials, Wiley [123].

Nordheim plot in Figure 9(c). The large enhancement factor has been attributed to the high aspect ratio of SWNT, which is greater than that of the conventional metallic emitter. In particular, the high field localization and short excitation wavelength enabled the generation of a narrow bandwidth in the kinetic energy (~0.25 eV) of the photo-induced electrons, as shown in Figure 9(d). The large enhancement factor enabled Keldysh parameters of $\gamma \sim 0.7$ at 820 nm and $\gamma \sim 2$ at 410 nm, indicating the strong tunneling regime, required for the subcycle emission. Studies on conventional metal tips typically focus on longer wavelengths because a higher power condition is required for a shorter wavelength to achieve comparable values of the Keldysh parameter (see Figure 9(e)).

C. High nonlinearity photoemission in SWNT

A nonlinear strong-field photoemission has recently been reported with a curve slope of up to the power of 40 for a semiconducting SWNT emitter, as shown in Figure 10(a) [124]. The emission has been attributed to optical-field-driven electron tunneling from the valence band of the SWNT. In comparison, such high nonlinearity has not been observed in a metallic SWNT (Figure 10(b)). Additionally, by using the laser with carrier envelop phase (CEP)-stabilization (7 fs pulse duration at an 800 nm central wavelength), a strong CEP-sensitive modulation was observed, reaching almost 100% with a peak current of 2 nA. This provides more evidence of strong-field tunneling emission (See Figure 10(c)). Simpleman model calculations based on the SWNT electronic band structures revealed the transition point between the conduction state emission and the valence band emission, as shown in Figure 10(d), above which the strong nonlinearity can be observed. In addition, the nonlinearity increased as the SWNT bandgap increased, indicating that the field emission characteristics can be tuned by engineering the band structure of the emitter. This may prove useful for future applications in attosecond electronics and photonics.

D. Electronic control of ultrashort emission in SWNT

The photo-induced field emission in a SWNT device exhibits a switching operation due to gate-induced variations in the effective barrier height of the devices [109]. As illustrated in Figure 11(a), a planer field emission device was fabricated by incorporating a nanogap in the middle of the SWNT field effect transistor, using focused ion-beam milling. An atomic force microscopy image of the gap region is shown in Figure 11(b). The device has a typical device channel length (l_{ch}) of 5 μm and a nanogap size

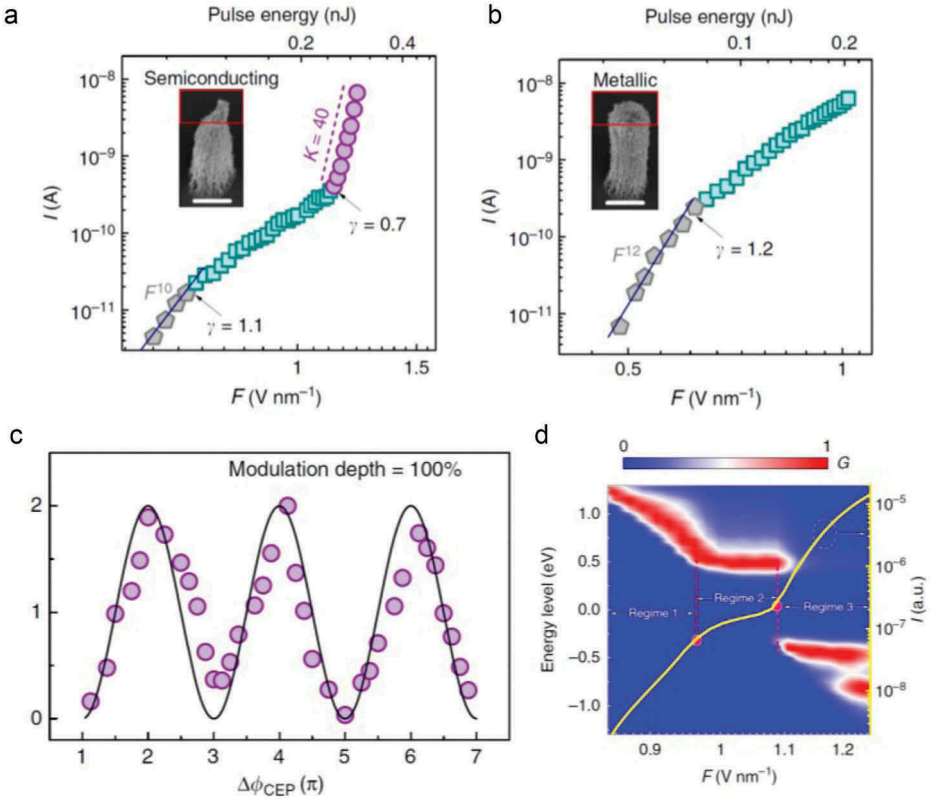

Figure 10. Power dependent photoemission from (a) semiconducting and (b) metallic SWNTs. (c) Modulation of photoemission through the carrier-envelop-phase (CEP) control (d) Simpleman model calculation of the emission yield as a function of the SWNT bandgap and the optical field strength. Copyright Nature Communications, Nature Publishing Group [124].

of 100 nm. In this case, the SWNT tip ends face each other, with one as the electron emitter and the other as the receiver. A strong photo-induced signal appeared when the focused laser illuminated the gap area of the device, for the back-gate bias of V_G= – 3 V, whereas the photoinduced signal is suppressed completely for V_G = 3.5 V, as shown in the bottom of Figure 11(c). This indicates that the electron emission yield can be manipulated by the gate electrode, which is used to tune the electronic state of SWNT (See also Figure 11(d)). The switching behaviors of the photoemission yield can be understood in the context of the band alignment of the SWNT devices, as schematically illustrated in Figure 11(e). Gate-dependent control of electron field emission has not been previously observed in investigations of photo-electron emissions and DC field emission systems. As a result, using the SWNT provides an added degree of freedom for controlling the electron emission yield and dynamic motion under the strong-field tunneling regime.

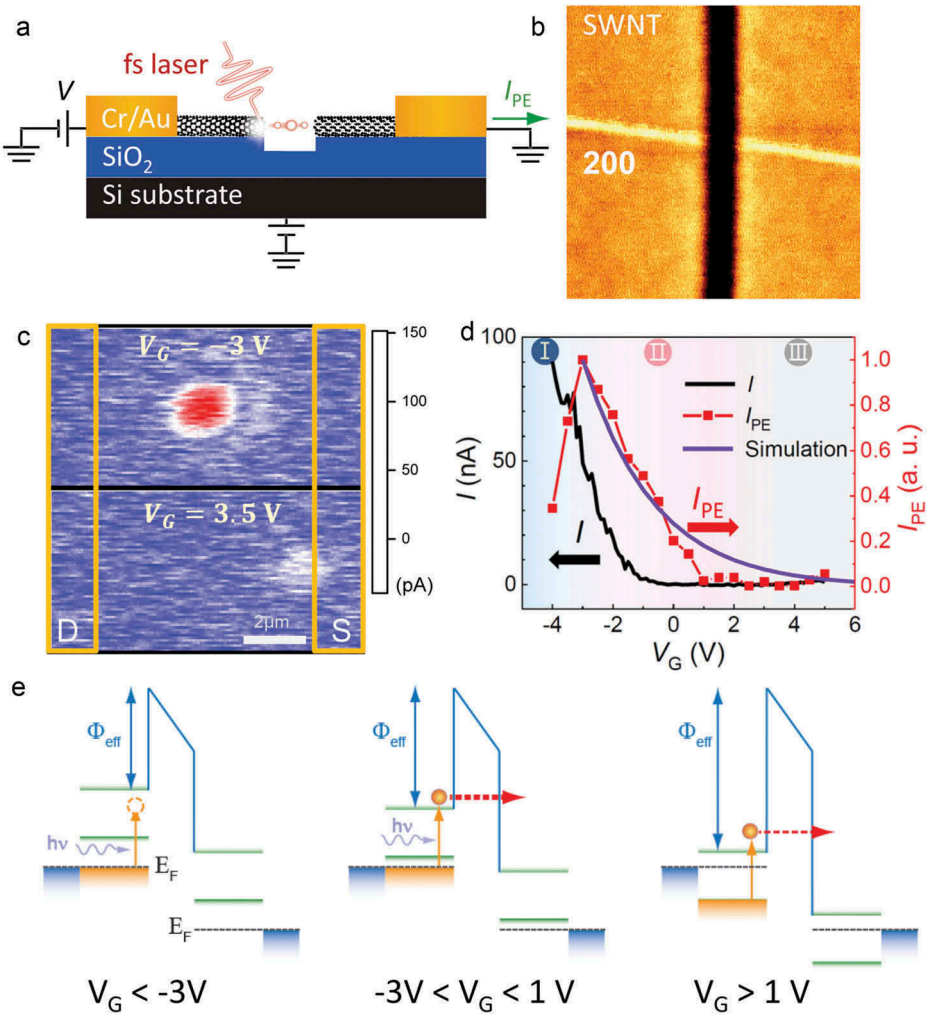

Figure 11. (a) Schematic of laser-field emission from the SWNT device with a nanogap. (b) AFM image of SWNT gap structure. (c) Scanning photocurrent image of photoelectrons from the SWNT nanogap. (d) Photoemission yield as a function of back-gate bias. (e) Schematic of photoelectron emission with a gate-dependent band alignment. Copyright Applied Physics Letters, American Institute of Physics [109].

IV. Strong-field photoemission in graphene

A. DC field emission in graphene

Low-dimensional carbon materials, such as graphene and CNTs, have nanoscale morphology, capable of producing high emission current density, due to their high damage threshold [74–77]. In particular, CNTs have been extensively investigated as alternative thermionic emitters. A Keldysh parameter of 0.67 has been recently demonstrated by irradiating fs laser pulses with a wavelength of 820 nm on CNTs, as mentioned above [123]. While CNTs have proven to be the most efficient materials for field emission

devices, a scalable process for precise selection and placement for CNTs has not yet been established. However, graphene has all the benefits of CNTs and is compatible with thin film processing. In particular, graphene edge, which has atomically thin morphology, could serve as an ideal platform for ultrafast field emission devices in the strong tunneling regime. This is due to its high aspect ratio, high carrier density, larger carrier mobility, and mechanical stability. Graphene-based DC field emitters have been recently demonstrated in the absence of illumination [76, 77, 125]; conversely, electron dynamics in the strong-field subcycle regime have also been recently demonstrated, using a femtosecond laser [126].

The DC field emission demonstrated on the graphene systems have been extensively reviewed in literature [125]. Field emission from graphene was initially reported for graphene flakes lying on or embedded in a substrate surface, which lacks the enhancement factor. However, graphene emitters with a form protruding from the surface result in a larger DC enhancement factor of 7300 [127]. Screen-printed graphene emitters with some vertical graphene sheets have a low turn-on electric field of 1.5 V·μm (1 μA·cm^{-2}), a low threshold field of 3.5 V·μm (1 mA·cm^{-2}) and an enhancement factor of 4539, as shown in Figure 12(a) [128]. Using structured polydimethylsiloxane (PDMS) stamps, a micro-transfer contact printing technique was developed; the results are illustrated in Figure 12(b). This technique can manipulate graphene into vertically standing fins on substrates [129].

To improve scalability in the fabrication of field emission devices, the nanogap structure has been fabricated from conventional graphene field-effect transistors [130]. Using electron-beam lithography, followed by an oxygen plasma process, the gaps on the suspended graphene conduction channel were fabricated, as shown in Figure 12(c). These devices show emission current densities in the range of tens of nA·μm^{-1} at modest bias voltages of tens of volts, as shown in Figure 12(d). The enhancement factors (of a few hundreds) and noise in the emission current (10%) are similar to those reported for single CNT field emitters. An application in pressure sensing was demonstrated by simply tracking changes in the emission current with pressure. Improvements in processing, e.g. decrease in nanogap dimension, will lead to higher performance. Such devices will not only enable nanoscale motion and chemical sensing but will also contribute to applications in electronics and fundamental studies of 2D materials.

B. Strong-field tunneling emission in graphene

Graphene has been recently demonstrated in an ultrafast electron emitter, specifically in the strong-field tunneling regime [71]. As schematically illustrated in Figure 13(a), graphene field emission devices were fabricated with a nanogap of 100 nm in the middle of the conducting channel, fabricated by

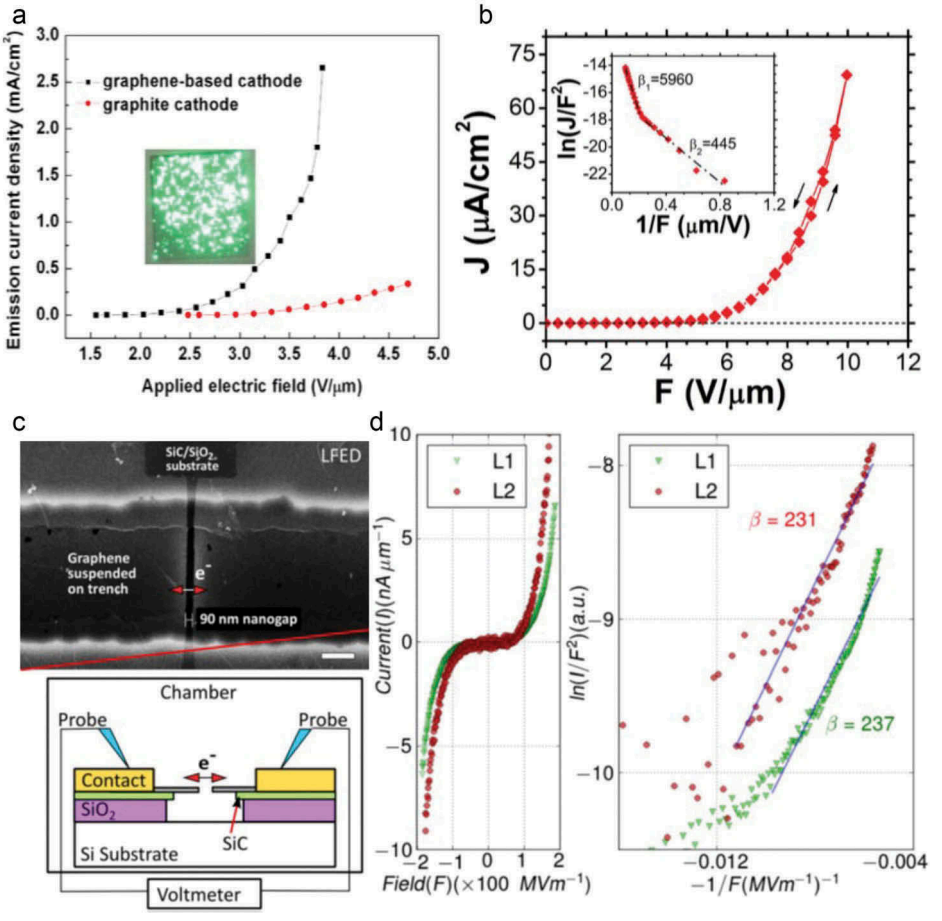

Figure 12. (a) DC field emission from the graphene flakes Copyright Nanotechnology, IOP Publishing [128] (b) Field emission from a patterned graphene fabricated by a contract printing technique Copyright Small, Wiley [129]. (c) and (d) Field emission device with a gap structure in the middle of graphene channel. Copyright Applied Physics Letters, American Institute of Physics [130].

focused ion beam (FIB) milling. In this scenario, two graphene edges facing each other across the nanogap, respectively, work as an electron emitter and receiver, similarly to the SWNT gap devices. The photo-assisted field emission was observed when the gap was illuminated by the fs laser pulse, as shown by a scanning photocurrent microscopy image [131–134] of a graphene device with a nanogap (inset of Figure 13(b)). Photoemission as a function of the bias exhibits a clear rectifying behavior, which is also confirmed by the Fowler–Nordheim plot. However, the turn-on voltage is reduced significantly with laser irradiation, which is due to the additional field-enhancement, supplied by the ultrashort laser pulse. The laser power dependence on photo-assisted field emission is plotted in Figure 13(b) (red circles). The significant tunneling current was possible due to the high

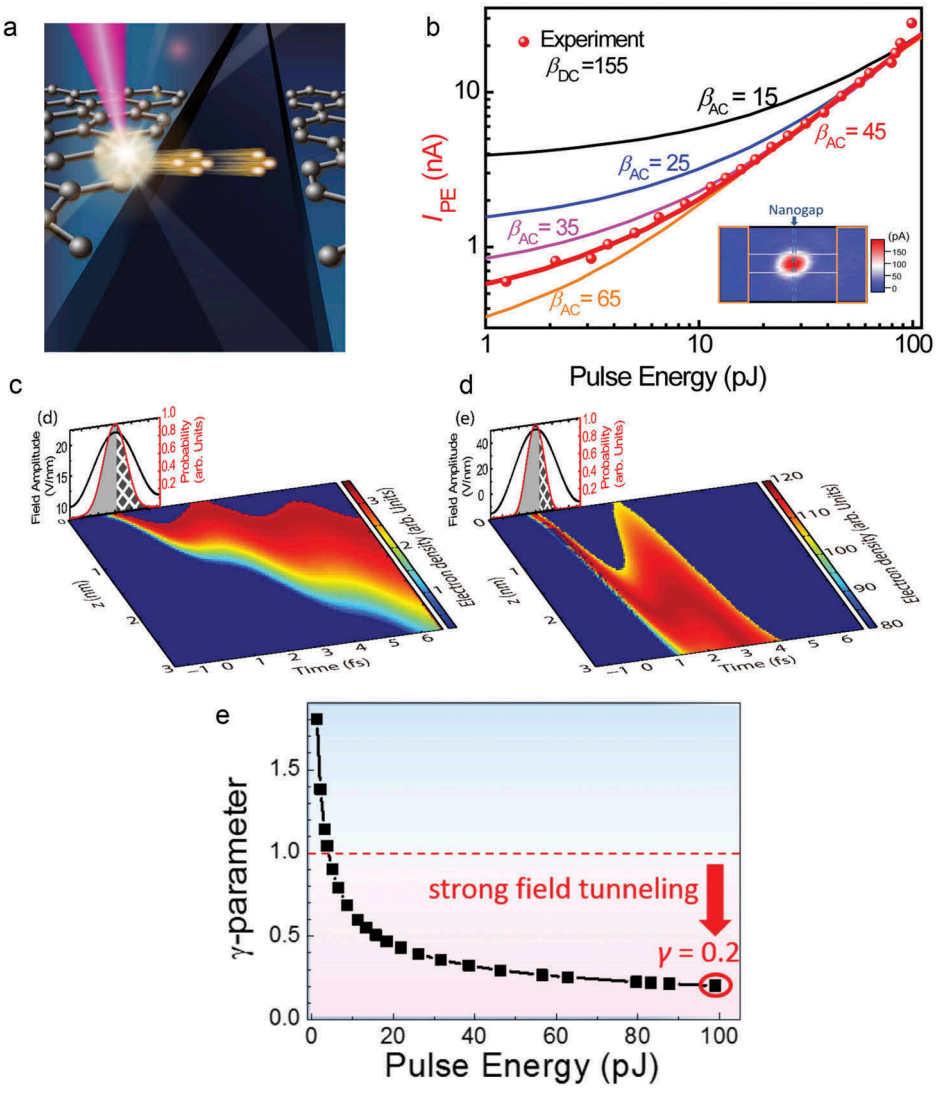

Figure 13. (a) Schematic of photoelectron emission in a graphene edge. (b) Electron emission yield as a function of laser power. (c) and (d) Simulation on the spatio-temporal electron probability for (c) low power and (d) high power conditions. (e) Keldysh parameter in the graphene edge emitter. Copyright ACS Photonics, American Chemical Society [71].

damage threshold of graphene. It is important to note that the photo-induced signals increase with increasing laser pulse energy, without demonstrating saturation behaviors. The unique nonlinear relationship, i.e. the increasing exponent with increasing power, is an indication of strong-field-assisted electron tunneling in the presence of a strong DC field, which is consistent with the theoretical prediction shown in Section II. A modified, quasi-classical Simpleman model [60–62] in the presence of strong DC

Table 1. Comparison of AC field enhancement factors and Keldysh parameters in the near-infrared range, with regard to field emission devices.

Materials	λ (nm)	*AC enhancement factor*	*Estimated field strength* (GV/m)	γ	Reference
Gold (tip)	3800	~10	28	0.13	[58]
Gold (tip)	1500	10	28	~0.3	[59]
Gold (tip)	830	8	23.5	~0.7	[55]
Tungsten (tip)	800	4.0	6.94	2.37	[57]
Silicon (tip)	800	14	15.4	1.12	[66]
SWNT	820	21.6	24.2	0.67	[111]
Graphene	800	45	77.8	0.2	[68]

fields has therefore successfully reproduced experimental results with the increasing nonlinearity.

In a spatio-temporal image for the simulated electron probability, a change in field strength induces a transition in the dynamic behavior, from the quiver motion to the subcycle motion, as shown in Figure 13(c,d). For the low-power condition, most of the electrons are in the quiver-motion regime; therefore, the electron wavepacket spreads over a large time duration. Conversely, in the high-power regime, more electrons exist in the subcycle regime, resulting in a shorter wavepacket. This result indicates that the high-power condition will allow us to produce trains of ultrafast electron wavepackets with a temporal width of less than the half-cycle of the incident laser pulses. The relative number of recoil electrons decreases in the high-intensity regime, allowing more electrons to escape from the strong near-field region before they are decelerated in the subsequent negative phase.

The device parameters for photoemission in various nanostructures are summarized in Table 1 for near-infrared illumination (~800 nm). As mentioned, the Keldysh parameter is one of the dominant factors that determine the dynamic behavior of photo-electrons; the strong-field emission dominates the emission process for $\gamma \ll 1$. Until now, the reported γ for the near-infrared range, with wavelength smaller than 1 μm $\lambda < 1$ μm, was ~0.7 for an SWNT vertical emitter and 0.2 for the single-layer graphene with a nanogap. For the graphene nanogap, the condition for $\gamma < 0.5$ can be reached at a very low pulse energy of $J \sim 15$ pJ, due to the large field enhancement factor, as shown in Figure 13(e). This is a sufficiently low value, reaching the deep tunneling regime [135], which will allow for electron emissions consistent with the subcycle wavepackets.

V. Conclusions and outlook

Ultrafast laser irradiation on metallic nanoprobes enabled highly efficient photoelectron emission with the help of field enhancement and field localization, the length scale of which is directly correlated to the dimension of the nanostructures. The interesting dynamic motion of photo-induced

electrons near the metallic nanotips have been realized both theoretically and experimentally. This may significantly contribute to the development of ultrashort electron sources. Recent progress has focused on increasing field electron emission with improved efficiency, achieving larger kinetic energy with improved ponderomotive acceleration, and adding more degrees of freedom to the control of electron emission. For example, the modification of nanotip morphology, by employing grating coupling techniques through adiabatic nanofocusing, improved the number of photoelectrons by up to 50 times compared to that of conventional metal tips. Coherent emission control with modulation of up to 94% was achieved with the simultaneous irradiation of two color lasers, which has been attributed to quantum-pathway interference. To achieve a low Keldysh parameter and high ponderomotive potential, a light source with a long wavelength is preferred. THz wave radiation on a metallic nanostructure have induced a photoelectron emission with an accelerated, monochromatic energy. In addition, various metallic structures such as nanorods and bowtie antenna have been introduced as efficient platforms for strong-field emission, with the field enhancement factor increasing to 50 in the case of the bow-tie structure.

Recently, low-dimensional carbon materials, such as the CNTs and graphenes, have emerged as promising candidates for strong-field tunneling emission, due to their high electrical conductivity, high damage threshold, chemical stability, and high aspect ratio. Strong-field tunneling emission has been demonstrated for light irradiation with a relatively short wavelength, enabling the generation of photoelectrons with a narrow bandwidth (~0.25 eV). In addition, electronic control over the SWNT band structure added a degree of freedom to the control of the electron emission yield, and possibly, their dynamic motion. Finally, a significant tunneling current was obtained by irradiating a graphene nanogap structure with a NIR laser. In this case, the emission yield exhibited an anomalous increase of nonlinear order as a function of the laser power. The simulated spatio-temporal image for electron probability revealed the transition of the dynamic behaviors, from quiver motion to the strong subcycle pulse generation, as a function of the field strength. This showed that the use of low-dimensional carbon materials enabled the generation of subcycle wavepackets, in which the emission yield, and potentially their dynamic behavior, can be efficiently manipulated.

The current pursuit for stable, efficient, and controllable emission sources via strong-field tunneling will pave the way for future applications, such as ultrafast spatio-temporal imaging microscopy, table-top scale attosecond streaking, and next-generation EUV sources. Specifically, recent achievements in the application of nanotips to ultrafast electron microscopy,

electron energy loss spectroscopy, and ultrafast low energy electron diffraction systems are noteworthy as a first step toward the development of novel instruments with ultrafast subcycle wavepackets. The streaking of THz waves using ultrafast electron wavepackets is also significant; the further development of highly monochromatic electron sources may lead to true table-top attosecond streaking within a sub-femtosecond resolution. As previously demonstrated, a large field enhancement near the nanostructure will guarantee high-energy EUV generation with a relatively lower laser power. Due to continually expanding industrial needs, investigation of strong-field photoemission in various nanostructures, and related research topics, will significantly impact the development of next-generation EUV sources.

Disclosure statement

No potential conflict of interest was reported by the authors.

Funding

This work was supported by the Midcareer Researcher Program (2017R1A2B4009177) and Small Grant for Exploratory Research Program (NRF-2018R1D1A1A02086036) of the Korea National Research Foundation grant funded by Korea Government; and by Human Resources Program in Energy Technology (20164030201380) of the Korea Institute of Energy Technology Evaluation and Planning (KETEP) grant funded by Korea Government (MOTIE).

ORCID

D. J. Park http://orcid.org/0000-0001-6816-5862

References

[1] Paul PM, Toma ES, Breger P, et al. Observation of a train of attosecond pulses from high harmonic generation. Science. 2001;292:1689–1692.
[2] Lewenstein M, Balcou P, Ivanov MY, et al. Theory of high-harmonic generation by low-frequency laser fields. Phys Rev A. 1994;49:2117–2132.
[3] Christov IP, Murnane MM, Kapteyn HC. High-harmonic generation of attosecond pulses in the "single-cycle" regime. Phys Rev Lett. 1997;78:1251–1254.
[4] Luu TT, Garg M, Kruchinin SY, et al. Extreme ultraviolet high-harmonic spectroscopy of solids. Nature. 2015;521:498.
[5] Chen MC, Gerrity MR, Backus S, et al. Spatially coherent, phase matched, high-order harmonic EUV beams at 50 kHz. Opt Express. 2009;17:17376–17383.
[6] Takahashi EJ, Nabekawa Y, Midorikawa K. Low-divergence coherent soft x-ray source at 13 nm by high-order harmonics. Appl Phys Lett. 2004;84:4–6.
[7] Bartels RA, Paul A, Green H, et al. Generation of spatially coherent light at extreme ultraviolet wavelengths. Science. 2002;297:376–378.

[8] Najafi E, Scarborough TD, Tang J, et al. Four-dimensional imaging of carrier interface dynamics in p-n junctions. Science. 2015;347:164–167.
[9] Herink G, Kurtz F, Jalali B, et al. Real-time spectral interferometry probes the internal dynamics of femtosecond soliton molecules. Science. 2017;356:50–54.
[10] Corkum PB, Krausz F. Attosecond science. Nat Phys. 2007;3:381–387.
[11] Gaarde MB, Tate JL, Schafer KJ. Macroscopic aspects of attosecond pulse generation. J Phys B. 2008;41:132001.
[12] Kim KT, Kim CM, Baik M-G, et al. Single sub-50- attosecond pulse generation from chirp-compensated harmonic radiation using material dispersion. Phys Rev A. 2004;69:051805.
[13] Chini M, Zhao K, Chang Z. The generation, characterization and applications of broadband isolated attosecond pulses. Nat Photonics. 2014;8:178.
[14] Ferrari F, Calegari F, Lucchini M, et al. High-energy isolated attosecond pulses generated by above-saturation few-cycle fields. Nat Photonics. 2010;4:875–879.
[15] Dudovich N, Smirnova O, Levesque J, et al. Measuring and controlling the birth of attosecond XUV pulses. Nat Phys. 2006;2:781–786.
[16] McPherson A, Gibson G, Jara H, et al. Studies of multiphoton production of vacuum-ultraviolet radiation in the rare gases. J Opt Soc Am B. 1987;4:595–601.
[17] Itatani J, Quéré F, Yudin GL, et al. Attosecond streak camera. Phys Rev Lett. 2002;88:173903.
[18] Eckle P, Smolarski M, Schlup P, et al. Attosecond angular streaking. Nat Phys. 2008;4:565–570.
[19] Cavalieri AL, Müller N, Uphues T, et al. Attosecond spectroscopy in condensed matter. Nature. 2007;449:1029–1032.
[20] Goulielmakis E, Yakovlev VS, Cavalieri AL, et al. Attosecond control and measurement: lightwave electronics. Science. 2007;317:769–775.
[21] Gaumnitz T, Jain A, Pertot Y, et al. Streaking of 43-attosecond soft-X-ray pulses generated by a passively CEP-stable mid-infrared driver. Opt Express. 2017;25:27506–27518.
[22] Eckle P, Pfeiffer AN, Cirelli C, et al. Attosecond ionization and tunneling delay time measurements in helium. Science. 2008;322:1525–1529.
[23] Stockman MI, Kling MF, Kleineberg U, et al. Attosecond nanoplasmonic-field microscope. Nat Photonics. 2007;1:539–544.
[24] Krausz F, Stockman MI. Attosecond metrology: from electron capture to future signal processing. Nat Photonics. 2014;8:205.
[25] Vogelgesang S, Storeck G, Horstmann JG, et al. Phase ordering of charge density waves traced by ultrafast low-energy electron diffraction. Nat Phys. 2018;14:184–190.
[26] Corkum PB. Plasma perspective on strong field multiphoton ionization. Phys Rev Lett. 1993;71:1994–1997.
[27] Schafer KJ, Yang B, DiMauro LF, et al. Above threshold ionization beyond the high harmonic cutoff. Phys Rev Lett. 1993;70:1599–1602.
[28] Corkum PB, Burnett NH, Brunel F. Above-threshold ionization in the long-wavelength limit. Phys Rev Lett. 1989;62:1259–1262.
[29] Walker B, Sheehy B, DiMauro LF, et al. Precision measurement of strong field double ionization of helium. Phys Rev Lett. 1994;73:1227–1230.
[30] Blaga CI, Catoire F, Colosimo P, et al. Strong-field photoionization revisited. Nat Phys. 2009;5:335–338.
[31] Kelldysh LV. Ionization in the field of a strong electromagnetic wave. J Exp Theor Phys. 1965;20:1307.

[32] Ciappina MF, Pérez-Hernández JA, Landsman AS, et al. Attosecond physics at the nanoscale. Rep Prog Phys. 2017;80:054401.
[33] Kienberger R, Uiberacker M, Goulielmakis E, et al. Single sub-fs soft-X-ray pulses: generation and measurement with the atomic transient recorder. J Mod Opt. 2005;52:261–275.
[34] Stupakov GV, Zolotorev MS. Ponderomotive laser acceleration and focusing in vacuum for generation of attosecond electron bunches. Phys Rev Lett. 2001;86:5274–5277.
[35] Malka G, Miquel JL. Experimental confirmation of ponderomotive-force electrons produced by an ultrarelativistic laser pulse on a solid target. Phys Rev Lett. 1996;77:75–78.
[36] Moore CI, Ting A, McNaught SJ, et al. A laser-accelerator injector based on laser ionization and ponderomotive acceleration of electrons. Phys Rev Lett. 1999;82:1688–1691.
[37] Kelkensberg F, Koenderink AF, Vrakking MJJ. Attosecond streaking in a nano-plasmonic field. New J Phys. 2012;14:093034.
[38] Baum P, Zewail AH. Attosecond electron pulses for 4D diffraction and microscopy. Proc Nat Acad Sci. 2007;104:18409–18414.
[39] Ebbesen TW, Lezec HJ, Ghaemi HF, et al. Extraordinary optical transmission through sub-wavelength hole arrays. Nature. 1998;391:667–669.
[40] Kim DS, Hohng SC, Malyarchuk V, et al. Microscopic origin of surface-plasmon radiation in plasmonic band-gap nanostructures. Phys Rev Lett. 2003;91:143901.
[41] Klar T, Perner M, Grosse S, et al. Surface-plasmon resonances in single metallic nanoparticles. Phys Rev Lett. 1998;80:4249–4252.
[42] Kawata S, Inouye Y, Verma P. Plasmonics for near-field nano-imaging and superlensing. Nat Photonics. 2009;3:388–394.
[43] Schröter U, Heitmann D. Surface-plasmon-enhanced transmission through metallic gratings. Phys Rev B. 1998;58:15419–15421.
[44] Barnes WL, Dereux A, Ebbesen TW. Surface plasmon subwavelength optics. Nature. 2003;424:824–830.
[45] Stiles PL, Dieringer JA, Shah NC, et al. Surface-enhanced Raman spectroscopy. Ann Rev Anal Chem. 2008;1:601–626.
[46] Kneipp K, Wang Y, Kneipp H, et al. Single molecule detection using Surface-Enhanced Raman Scattering (SERS). Phys Rev Lett. 1997;78:1667–1670.
[47] Stöckle RM, Suh YD, Deckert V, et al. Nanoscale chemical analysis by tip-enhanced Raman spectroscopy. Chem Phys Lett. 2000;318:131–136.
[48] Stefani FD, Vasilev K, Bocchio N, et al. Surface-plasmon-mediated single-molecule fluorescence through a thin metallic film. Phys Rev Lett. 2005;94:023005.
[49] Aćimović SS, Kreuzer MP, González MU, et al. Plasmon near-field coupling in metal dimers as a step toward single-molecule sensing. ACS Nano. 2009;3:1231–1237.
[50] Smith DR, Pendry JB, Wiltshire MCK. Metamaterials and negative refractive index. Science. 2004;305:788–792.
[51] Schurig D, Mock JJ, Justice BJ, et al. Metamaterial electromagnetic cloak at microwave frequencies. Science. 2006;314:977–980.
[52] Pendry JB. Negative refraction makes a perfect lens. Phys Rev Lett. 2000;85:3966–3969.
[53] Alù A, Silveirinha MG, Salandrino A, et al. Epsilon-near-zero metamaterials and electromagnetic sources: tailoring the radiation phase pattern. Phys Rev B. 2007;75:155410.

[54] Alam MZ, De Leon I, Boyd RW. Large optical nonlinearity of indium tin oxide in its epsilon-near-zero region. Science. 2016;352:795–797.
[55] Ropers C, Solli DR, Schulz CP, et al. Localized multiphoton emission of femtosecond electron pulses from metal nanotips. Phys Rev Lett. 2007;98:043907.
[56] Hommelhoff P, Sortais Y, Aghajani-Talesh A, et al. Field emission tip as a nanometer source of free electron femtosecond pulses. Phys Rev Lett. 2006;96:077401.
[57] Schenk M, Krüger M, Hommelhoff P. Strong-field above-threshold photoemission from sharp metal tips. Phys Rev Lett. 2010;105:257601.
[58] Bormann R, Gulde M, Weismann A, et al. Tip-enhanced strong-field photoemission. Phys Rev Lett. 2010;105:147601.
[59] Yalunin SV, Herink G, Solli DR, et al. Field localization and rescattering in tip-enhanced photoemission. Ann Phys. 2013;525:L12–L18.
[60] Krüger M, Schenk M, Hommelhoff P. Attosecond control of electrons emitted from a nanoscale metal tip. Nature. 2011;475:78–81.
[61] Herink G, Solli DR, Gulde M, et al. Field-driven photoemission from nanostructures quenches the quiver motion. Nature. 2012;483:190–193.
[62] Park DJ, Piglosiewicz B, Schmidt S, et al. Strong field acceleration and steering of ultrafast electron pulses from a sharp metallic nanotip. Phys Rev Lett. 2012;109:244803.
[63] Piglosiewicz B, Schmidt S, Park DJ, et al. Carrier-envelope phase effects on the strong-field photoemission of electrons from metallic nanostructures. Nat Photonics. 2013;8:37.
[64] Schröder B, Weber T, Yalunin SV, et al. Real-space imaging of nanotip plasmons using electron energy loss spectroscopy. Phys Rev B. 2015;92:085411.
[65] Hommelhoff P, Kealhofer C, Kasevich MA. Ultrafast electron pulses from a tungsten tip triggered by low-power femtosecond laser pulses. Phys Rev Lett. 2006;97:247402.
[66] Vogelsang J, Robin J, Nagy BJ, et al. Ultrafast electron emission from a sharp metal nanotaper driven by adiabatic nanofocusing of surface plasmons. Nano Lett. 2015;15:4685–4691.
[67] Sivis M, Duwe M, Abel B, et al. Extreme-ultraviolet light generation in plasmonic nanostructures. Nat Phys. 2013;9:304.
[68] Kim S, Jin J, Kim Y-J, et al. High-harmonic generation by resonant plasmon field enhancement. Nature. 2008;453:757.
[69] Keathley PD, Sell A, Putnam WP, et al. Strong-field photoemission from silicon field emitter arrays. Ann Phys. 2013;525:144–150.
[70] Ward DR, Hüser F, Pauly F, et al. Optical rectification and field enhancement in a plasmonic nanogap. Nat Nanotechnol. 2010;5:732–736.
[71] Son BH, Kim HS, Park J-Y, et al. Ultrafast strong-field tunneling emission in graphene nanogaps. ACS Photonics. 2018;5:3943–3949.
[72] Park DJ, Piglosiewicz B, Schmidt S, et al. Characterizing the optical near-field in the vicinity of a sharp metallic nanoprobe by angle-resolved electron kinetic energy spectroscopy. Ann Phys. 2013;525:135–142.
[73] Zherebtsov S, Fennel T, Plenge J, et al. Controlled near-field enhanced electron acceleration from dielectric nanospheres with intense few-cycle laser fields. Nat Phys. 2011;7:656–662.
[74] Eletskii AV. Carbon nanotube-based electron field emitters. Physics-Uspekhi. 2010;53:863–892.
[75] Zhu W, Bower C, Zhou O, et al. Large current density from carbon nanotube field emitters. Appl Phys Lett. 1999;75:873–875.

[76] Kim T, Lee JS, Li K, et al. High performance graphene foam emitter. Carbon. 2016;101:345–351.
[77] Weiss NO, Zhou H, Liao L, et al. Graphene: an emerging electronic material. Adv Mater. 2012;24:5782–5825.
[78] Ropers C, Neacsu CC, Elsaesser T, et al. Grating-coupling of surface plasmons onto metallic tips: a nanoconfined light source. Nano Lett. 2007;7:2784–2788.
[79] Sadiq D, Shirdel J, Lee JS, et al. Adiabatic nanofocusing scattering-type optical nanoscopy of individual gold nanoparticles. Nano Lett. 2011;11:1609–1613.
[80] Krüger M, Lemell C, Wachter G, et al. Attosecond physics phenomena at nanometric tips. J Phys B. 2018;51:172001.
[81] Yalunin SV, Gulde M, Ropers C. Strong-field photoemission from surfaces: theoretical approaches. Phys Rev B. 2011;84:195426.
[82] Ciappina MF, Pérez-Hernández JA, Shaaran T, et al. Electron-momentum distributions and photoelectron spectra of atoms driven by an intense spatially inhomogeneous field. Phys Rev A. 2013;87:063833.
[83] Pant M, Ang LK. Ultrafast laser-induced electron emission from multiphoton to optical tunneling. Phys Rev B. 2012;86:045423.
[84] Wopperer P, De Giovannini U, Rubio A. Efficient and accurate modeling of electron photoemission in nanostructures with TDDFT. Eur Phys J B. 2017;90:51.
[85] Giugni A, Allione M, Torre B, et al. Adiabatic nanofocusing: spectroscopy, transport and imaging investigation of the nano world. J Opt. 2014;16:114003.
[86] Vernon KC, Gramotnev DK, Pile DFP. Adiabatic nanofocusing of plasmons by a sharp metal wedge on a dielectric substrate. J Appl Phys. 2007;101:104312.
[87] Stockman MI. Nanofocusing of optical energy in tapered plasmonic waveguides. Phys Rev Lett. 2004;93:137404.
[88] Vogelsang J, Hergert G, Wang D, et al. Observing charge separation in nanoantennas via ultrafast point-projection electron microscopy. Light Sci Appl. 2018;7:55.
[89] Schröder B, Sivis M, Bormann R, et al. An ultrafast nanotip electron gun triggered by grating-coupled surface plasmons. Appl Phys Lett. 2015;107:231105.
[90] Thomas S, Wachter G, Lemell C, et al. Large optical field enhancement for nanotips with large opening angles. New J Phys. 2015;17:063010.
[91] Förster M, Paschen T, Krüger M, et al. Two-color coherent control of femtosecond above-threshold photoemission from a Tungsten nanotip. Phys Rev Lett. 2016;117:217601.
[92] Seiffert L, Paschen T, Hommelhoff P, et al. High-order above-threshold photoemission from nanotips controlled with two-color laser fields. J Phys B. 2018;51:134001.
[93] Herink G, Wimmer L, Ropers C. Field emission at terahertz frequencies: AC-tunneling and ultrafast carrier dynamics. New J Phys. 2014;16:123005.
[94] Wimmer L, Herink G, Solli DR, et al. Terahertz control of nanotip photoemission. Nat Phys. 2014;10:432.
[95] Zewail AH. Four-dimensional electron microscopy. Science. 2010;328:187–193.
[96] Baum P, Zewail AH. Breaking resolution limits in ultrafast electron diffraction and microscopy. Proc Nat Acad Sci. 2006;103:16105–16110.
[97] Teichmann SM, Rácz P, Ciappina MF, et al. Strong-field plasmonic photoemission in the mid-IR at <1 GW/cm2 intensity. Sci Rep. 2015;5:7584.
[98] Budai J, Pápa Z, Márton I, et al. Plasmon–plasmon coupling probed by ultrafast, strong-field photoemission with <7 Å sensitivity. Nanoscale. 2018;10:16261–16267.
[99] Kusa F, Echternkamp KE, Herink G, et al. Optical field emission from resonant gold nanorods driven by femtosecond mid-infrared pulses. AIP Adv. 2015;5:077138.

[100] Sivis M, Pazos-Perez N, Yu R, et al. Continuous-wave multiphoton photoemission from plasmonic nanostars. Commun Phys. 2018;1:13.
[101] Putnam WP, Hobbs RG, Keathley PD, et al. Optical-field-controlled photoemission from plasmonic nanoparticles. Nat Phys. 2017;13:335–339.
[102] Keathley PD, Putnam WP, Vasireddy P, et al. Vanishing carrier-envelope-phase-sensitive response in optical-field photoemission from plasmonic nanoantennas. Nat Phys. 2019;15:1128–1133.
[103] Mühlschlegel P, Eisler H-J, Martin OJF, et al. Resonant optical antennas. Science. 2005;308:1607–1609.
[104] Sivis M, Duwe M, Abel B, et al. Nanostructure-enhanced atomic line emission. Nature. 2012;485:E1–E2.
[105] Kim S, Jin J, Kim Y-J, et al. Reply. Nature. 2012;485:E2–E3.
[106] Dombi P, Hörl A, Rácz P, et al. Ultrafast strong-field photoemission from plasmonic nanoparticles. Nano Lett. 2013;13:674–678.
[107] Rácz P, Pápa Z, Márton I, et al. Measurement of nanoplasmonic field enhancement with ultrafast photoemission. Nano Lett. 2017;17:1181–1186.
[108] Rybka T, Ludwig M, Schmalz MF, et al. Sub-cycle optical phase control of nanotunnelling in the single-electron regime. Nat Photonics. 2016;10:667–670.
[109] Son BH, Park DJ, Ahn YH. Electronic control of ultrafast field emission in carbon nanotube gaps. Appl Phys Lett. 2019;115:163102.
[110] Yanagisawa H, Schnepp S, Hafner C, et al. Delayed electron emission in strong-field driven tunnelling from a metallic nanotip in the multi-electron regime. Sci Rep. 2016;6:35877.
[111] Zhang P, Lau YY. Ultrafast strong-field photoelectron emission from biased metal surfaces: exact solution to time-dependent Schrödinger equation. Sci Rep. 2016;6:19894.
[112] Zhou S, Chen K, Cole MT, et al. Ultrafast field-emission electron sources based on nanomaterials. Adv Mater. 2019;31:1805845.
[113] Park DJ, Ahn YH. Development of a theoretical model for strong-field photoemission in a 2-dimensional conducting sheet. J Korean Phys Soc. 2019;75:882–886.
[114] Tong A, Zhou Y, Lu P. Resolving subcycle electron emission in strong-field sequential double ionization. Opt Express. 2015;23:15774–15783.
[115] Li Y, Sun Y, Yeow JTW. Nanotube field electron emission: principles, development, and applications. Nanotechnology. 2015;26:242001.
[116] Prasek J, Drbohlavova J, Chomoucka J, et al. Methods for carbon nanotubes synthesis—review. J Mater Chem. 2011;21:15872–15884.
[117] Szabó A, Perri C, Csató A, et al. Synthesis methods of carbon nanotubes and related materials. Materials. 2010;3:3092–3140.
[118] de Heer WA, Châtelain A, Ugarte D. A carbon nanotube field-emission electron source. Science. 1995;270:1179–1180.
[119] Pirio G, Legagneux P, Pribat D, et al. Fabrication and electrical characteristics of carbon nanotube field emission microcathodes with an integrated gate electrode. Nanotechnology. 2001;13:1–4.
[120] Jung SI, Choi JS, Shim HC, et al. Fabrication of probe-typed carbon nanotube point emitters. Appl Phys Lett. 2006;89:233108.
[121] Lim SC, Lee DS, Choi HK, et al. Field emission of carbon-nanotube point electron source. Diam Relat Mater. 2009;18:1435–1439.
[122] Song X, Gao J, Fu Q, et al. Novel planar field emission of ultra-thin individual carbon nanotubes. Nanotechnology. 2009;20:405208.

[123] Li C, Zhou X, Zhai F, et al. Carbon nanotubes as an ultrafast emitter with a narrow energy spread at optical frequency. Adv Mater. 2017;29:1701580.
[124] Li C, Chen K, Guan M, et al. Extreme nonlinear strong-field photoemission from carbon nanotubes. Nat Commun. 2019;10:4891.
[125] Chen L, Yu H, Zhong J, et al. Graphene field emitters: A review of fabrication, characterization and properties. Mater Sci Eng B. 2017;220:44–58.
[126] Higuchi T, Heide C, Ullmann K, et al. Light-field-driven currents in graphene. Nature. 2017;550:224.
[127] Dong J, Zeng B, Lan Y, et al. Field emission from few-layer graphene nanosheets produced by liquid phase exfoliation of graphite. J Nanosci Nanotechnol. 2010;10:5051–5055.
[128] Qian M, Feng T, Ding H, et al. Electron field emission from screen-printed graphene films. Nanotechnology. 2009;20:425702.
[129] Hallam T, Cole MT, Milne WI, et al. Field emission characteristics of contact printed graphene fins. Small. 2014;10:95–99.
[130] Kumar S, Duesberg GS, Pratap R, et al. Graphene field emission devices. Appl Phys Lett. 2014;105:103107.
[131] Ahn YH, Tsen AW, Kim B, et al. Photocurrent imaging of p–n junctions in ambipolar carbon nanotube transistors. Nano Lett. 2007;7:3320–3323.
[132] Park J, Ahn YH, Ruiz-Vargas C. Imaging of photocurrent generation and collection in single-layer graphene. Nano Lett. 2009;9:1742–1746.
[133] Park JK, Son BH, Park J-Y, et al. Imaging surface charge distribution near carbon nanotube device in aqueous environments. Appl Phys Lett. 2014;105:223101.
[134] Son BH, Park J-K, Hong JT, et al. Imaging ultrafast carrier transport in nanoscale field-effect transistors. ACS Nano. 2014;8:11361–11368.
[135] Ilkov FA, Decker JE, Chin SL. Ionization of atoms in the tunnelling regime with experimental evidence using Hg atoms. J Phys B. 1992;25:4005–4020.